Journal of Zhejiang University-SCIENCE A (Applied Physics & Engineering) 2024 25(3):206-222
www.jzus.zju.edu.cn; www.springer.com/journal/11582
E-mail: jzus_a@zju.edu.cn

Research Article
https://doi.org/10.1631/jzus.A2300085

A method for support stiffness failure identification in a steel spring floating slab track of urban railway: a case study in China

Junyuan ZHENG[1,2], Caiyou ZHAO[1,2]✉, Duojia SHI[1,2], Ping WANG[1,2], Jian WANG[3], Bolong JIANG[4], Xi SHENG[5]

[1]*Key Laboratory of High-speed Railway Engineering, Ministry of Education, Southwest Jiaotong University, Chengdu 610031, China*
[2]*School of Civil Engineering, Southwest Jiaotong University, Chengdu 610031, China*
[3]*01 DYNA (Qingdao) Test & Data Co., Ltd., Qingdao 266000, China*
[4]*Rail Transit Digital Construction and Measurement Technology National Engineering Research Center, China Railway Design Corporation, Tianjin 300308, China*
[5]*Institute of Urban Smart Transportation & Safety Maintenance, Shenzhen University, Shenzhen 518060, China*

Abstract: The extensive use of steel spring floating slab tracks has effectively addressed the challenge of alleviating the environmental vibrations induced by urban rail transit systems. However, under the combined action of train dynamic loads and complex environmental factors, problems, such as the fracture of steel spring vibration isolators and suspension vibrations induced by the uneven settlement of the base, often occur. The failure of isolator support stiffness is often hidden in its early stages and is challenging to identify by conventional detection methods. At the same time, it will aggravate the wheel–rail interaction, accelerate the deterioration of track structure, and even affect the driving safety. This study first establishes a detailed coupled train-floating slab track-foundation analytical model. Then the influence of the vibration isolator support stiffness failure on the dynamic indices of the floating slab track system response is analyzed. A set of defect identification methods that can detect the number of failed steel springs, severity of damage, and their location is proposed. Finally, an intelligent monitoring system for support stiffness of floating slab track is built by combining the density-based spatial clustering of applications with noise algorithm and statistical data analysis and is applied to a rail line in southern China. During a three-year monitoring campaign, a suspension failure and a fracture of a steel spring were each successfully detected and detailed failure information was obtained. Field investigation results were consistent with the damage identification results. After repair, the track structure dynamic response returned to the average pre-damage level and further deterioration had been arrested. The proposed damage identification methods and monitoring system provide an approach for intelligent identification of track structure support stiffness failures.

Key words: Floating slab track; Support stiffness; Detailed analytical model; Failure identification; Monitoring system

1 Introduction

With the increase in train line length and train speeds, the environmental vibrations caused by urban rail transit systems are becoming increasingly serious. Vibration reduction measures for metro lines can be divided into three types according to their different implementation locations. At the vibration source, many measures, such as floating slab track bed (Tamagawa, 2021), damping fasteners (Cui et al., 2016), and elastic sleepers (Auersch, 2017), can be used to weaken the propagation of vibration energy at the wheel–rail contact location and thus reduce the vibration energy input to the soil. Along the propagation path, vibration isolation trenches (Sitharam et al., 2018) and rigid barriers can be used for vibration isolation. Measures such as foundation isolation systems (Talbot, 2016) can be introduced for vibration control. The control measures at the vibration source reduce the outward spreading of vibration energy from the source and are more widely used. The floating slab track bed has a better vibration reduction performance than other measures applied at the vibration source. In the floating slab track bed, instead of the traditional cast-in-place track bed and

✉ Caiyou ZHAO, zcy848279@163.com
Junyuan ZHENG, https://orcid.org/0000-0001-5203-3136
Duojia SHI, https://orcid.org/0000-0001-5081-7973

Received Feb. 14, 2023; Revision accepted June 26, 2023;
Crosschecked Jan. 3, 2024

foundation, a track slab elastically supported by steel springs (Bashir and Akhtar, 2022) or rubber pads (Yuan et al., 2020) is adopted. The basic structure is shown in Fig. 1. The existence of elastic support makes the inertia of the floating slab absorb the dynamic train loads and reduce the vibration transmission from the track to the substructure (Wilson et al., 1983).

Although steel spring floating slabs have the best vibration isolation effect, up to 30 dB (Zou et al., 2022), many studies have recently attempted to further improve their performance (Nelson et al., 2018; Wang et al., 2022). However, the steel springs not only damp vibrations but also carry all the static and dynamic loads of trains and the track. In addition to determining the vibration damping performance, their condition directly affects the running condition and even the running safety of trains. There is currently a lot of research on track support failure. Dersch et al. (2021) proposed reducing fastener failure through parameter optimization using a finite element method but did not conduct an experimental verification. Yu et al. (2021) studied the pull-out resistance of different materials of sleepers and proposed a prediction formula for pull-out resistance. Lam et al. (2012) studied the relationship between ballast damage and sleeper vibration, providing ideas for damage detection. Ramos et al. (2021) compared the settlement performance of ballast and slab railway track structures in the laboratory and obtained consistent numerical results.

However, relatively little research has been conducted on the failure of steel springs in floating slab track. Xu et al. (2020) established a 2D coupled train-floating slab track model and analyzed the influence of the number of failed springs on soil vibrations in combination with a finite element model. However, their model did not consider the spatial distribution of failed springs. Zhao et al. (2019) established a 3D coupled train-floating slab-track dynamic model, studied the effect of spring failure location on the train track dynamic responses, and concluded that spring failures at the slab ends are more harmful to driving safety and environmental vibrations.

The above studies mainly focused on the adverse effects of steel spring failures. These harmful effects can be avoided if the spring failure is detected early. Generally, structural damage detection methods analyze the dynamic responses of the structure and detect structural damage from changes in the natural frequencies (Dilena et al., 2015), modal shapes (Gomes and Giovani, 2022), or flexibility matrix (Wickramasinghe et al., 2020). However, these approaches have several shortcomings (Zhu et al., 2021). For example, damage usually only affects the local response of the structure, which requires proper arrangement of sensors to be detectable. Modal shape measurement requires high accuracy and is easily affected by noise and human error. The flexibility matrix method requires prior knowledge of the undamaged structure.

In addition to these traditional monitoring methods, some novel detection methods have been studied and applied in rail transit. The identification of suspension has been extensively carried out in vehicles. Ankrah et al. (2020) used vehicle acceleration combined with a support vector machine to predict the fault state of suspension systems. Similarly, Hong et al. (2020) proposed a data-driven framework for identifying suspension

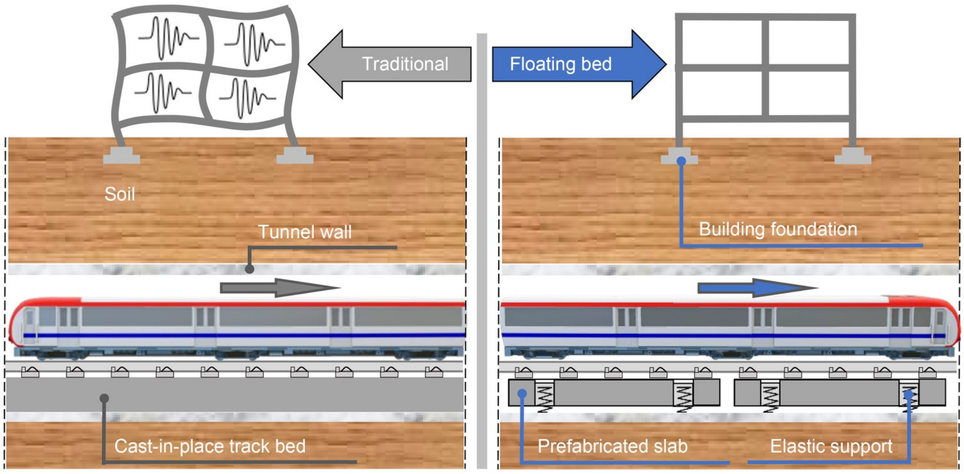

Fig. 1 Comparison between traditional track bed and floating slab track bed

system status through train vibration. Some scholars also use train vibration for track state evaluation (Cong et al., 2020), but separating the influence of suspension system and track state is a challenge which makes this method difficult for stiffness failure identification of steel springs. For the track structure, damage detection approaches frequently use visual, ultrasonic, or electromagnetic inspections for identifying rail damage (Loveday et al., 2020), fastener failure (Chandran et al., 2022), and track slab cracking (Li et al., 2020). However, these technologies require access to the inspected element surface, but the steel springs are wrapped by sleeves and are therefore inaccessible. The spring break indicator developed in recent years tries to address this challenge. If a steel spring is broken, an indicator light will switch on. However, the device has many shortcomings: each steel spring requires an individual indicator, the light will not turn on until a certain degree of fracture is reached, and the degree of suspension cannot be displayed. In addition, the light can only by detected by night patrols rather than monitored in real-time. Conventional vibration monitoring of track structure is easy to implement but signal anomaly detection is challenging. On the one hand, the conventional time-domain data change little, so it is difficult to identify failure whereas; on the other hand, the regular detection cycle is long and its time is short. Even if abnormal data are found, the failure may already be severe. If failure can be discovered early, the maintenance costs can be significantly reduced. Zhu et al. (2021) proposed a failure detection method based on a convolution neural network using the vibration data from a floating slab, but their approach required undamaged and damaged data sets, which is difficult to satisfy in the field.

This study presents a more straightforward method to identify the number, degree, and location of steel spring failures. Firstly, a refined train-floating slab track-foundation analytical model is established and the sensitivity of various floating slab dynamic response indices to failure is analyzed. Methods for identifying the failure of steel springs are proposed based on the specific sensitive dynamic response indices. Based on the proposed method, an intelligent monitoring system for the support stiffness of the floating slab track (ISFST) system was developed and applied in the field, where it detected steel spring failures. An on-site inspection confirmed the failure identification results. Furthermore, the monitoring data returned to normal pre-damage values after repairs. The structure of the proposed technology is shown in Fig. 2. Although steel spring support failure is studied in this paper, the proposed method will be applicable to other types of supports as well.

2 Detailed coupled train–floating slab track–foundation analytical model

The developed coupled train–floating slab track–foundation dynamic model comprises three subsystems: the train, the track, and the foundation, as shown in Fig. 3. X, Y, and Z refer to the translational directions. β, Ψ, and Φ refer to the rotational directions.

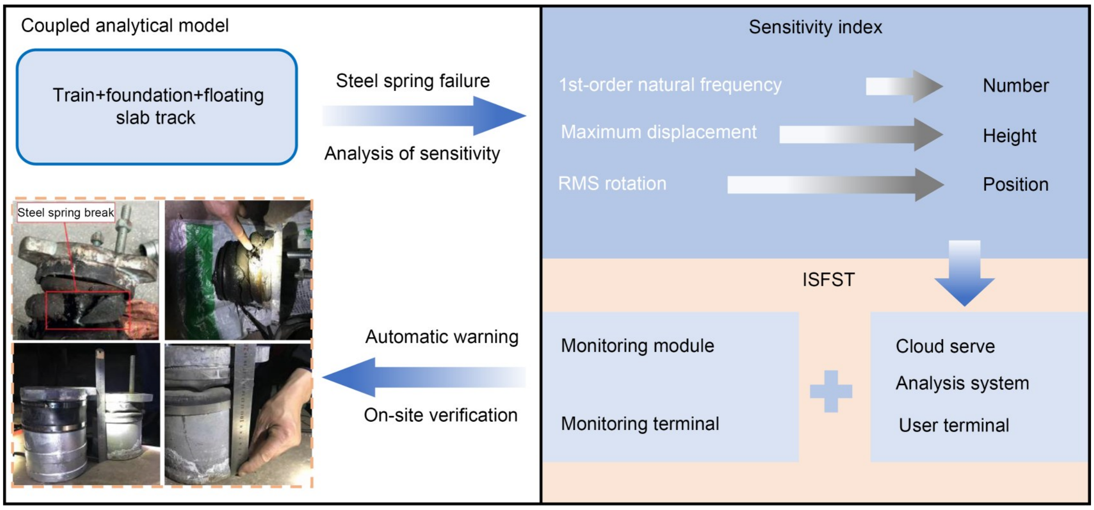

Fig. 2 Proposed technology structure. RMS: root mean square

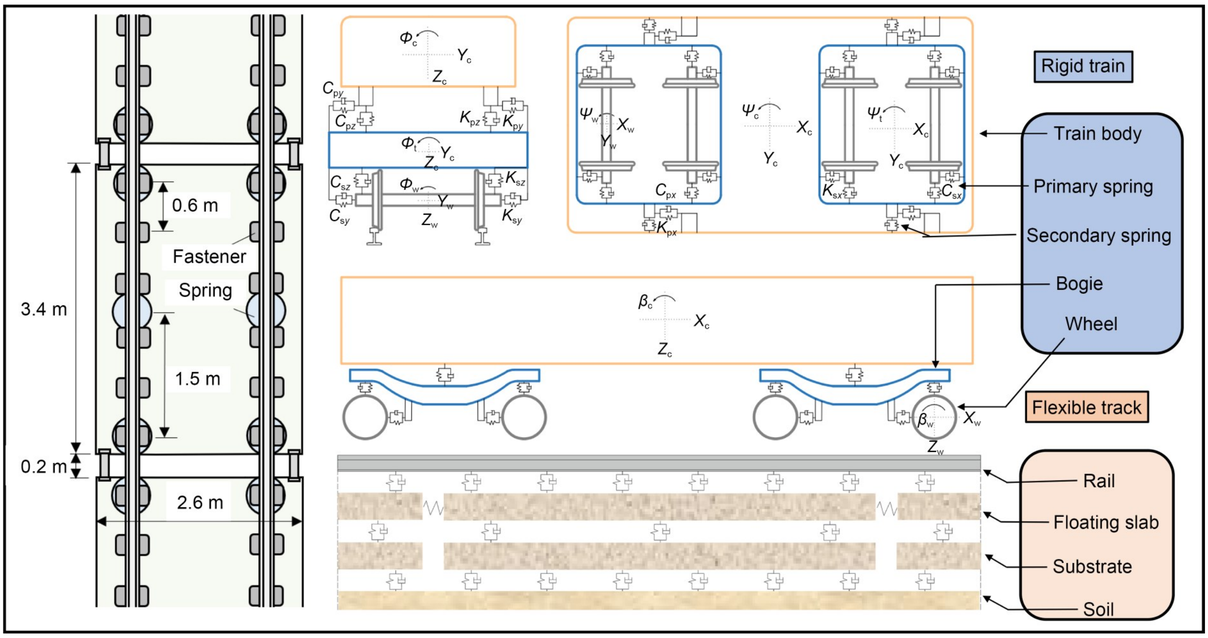

Fig. 3 Train structure

The subscripts c, w, and t refer to the train body, wheel, and bogie, respectively. The subscripts s and p refer to the first and second suspensions, respectively. The train is a multi-rigid body structure, while the track and foundation are flexible bodies. The train consists of six A-type vehicles, each consisting of a train body, two bogies, four wheelsets (Chinese LMA tread), and eight axle boxes. The train body and bogies have three translational and three rotational degrees of freedom (DOFs), while the wheelsets have two translational DOFs (the translation in the *X*-direction is realized through the specified train driving speed) and three rotational DOFs. The wheels and axle box are connected through primary springs and dashpots, and the bogies and train body are connected through secondary springs and dashpots. The train parameters are listed in Table 1. The track and foundation model comprise, from top to bottom, the rails, fasteners, floating slabs, steel springs, substrates, and soil. A Timoshenko beam was used to simulate the rail and the finite element method was adopted to model the floating slabs and foundation. The rail was connected to the floating slabs through the fasteners (6-DOF spring-dashpot elements), the floating slabs were connected to the foundation through steel springs (3-DOF spring-dashpot elements), and eventually the foundation was connected to the soil. The longitudinal spacing of fasteners was 0.6 m and the transverse spacing was 1.5 m. The longitudinal spacing of steel springs was 1.6 m, while the transverse spacing was 1.5 m. The slabs were connected by shear hinges (simulated by 3-DOF springs with a large stiffness) to ensure the consistency of slab end displacements.

The track parameters are listed in Table 2 and component connections are shown in Fig. 3. The total length of the track was 1200 m, including 35 floating slabs. The track irregularity was adopted from measured data in (Zhao et al., 2021). The coupling between the train and the track was realized through the wheel–rail contact. The wheel–rail normal force was determined according to the Hertz nonlinear contact theory, and then the creep force was calculated by the Kalker linear creep theory with a nonlinear correction (Shen et al., 1983). The modal superposition method was used to calculate the response of the track structure. The modal superposition method has good calculation efficiency, which can be guaranteed if the number of modes considered is large enough. As shown in Eq. (1), the normalized mode coordinate can be introduced to solve the associated motion equation. t is the time. $\boldsymbol{q}_{si}(t)$ refers to the displacement vector of the ith mode, and the total number of modes was 30 for slab, 30 for substrate, and 4000 for rail. $\tilde{\boldsymbol{M}}_s$, $\tilde{\boldsymbol{K}}_s$, and $\tilde{\boldsymbol{C}}_s$ denote the normalized mass matrix, stiffness matrix, and damping matrix, respectively. $\tilde{\boldsymbol{\Phi}}_s$ and $\tilde{\boldsymbol{F}}_s$ represent the normalized modal shape matrix and the external force vector, respectively.

Table 1 A-type train parameters

Parameter	Value
Mass of train body, M_{c} (t)	41.8
Mass moment of inertia of train body for roll, $I_{\mathrm{c}x}$ (t·m^2)	155
Mass moment of inertia of train body for pitch, $I_{\mathrm{c}y}$ (t·m^2)	1959
Mass moment of inertia of train body for yaw, $I_{\mathrm{c}z}$ (t·m^2)	1875
Mass of bogie, M_{t} (t)	7.36
Mass moment of inertia of bogie for roll, $I_{\mathrm{t}x}$ (t·m^2)	5.07
Mass moment of inertia of bogie for pitch, $I_{\mathrm{t}y}$ (t·m^2)	1.47
Mass moment of inertia of bogie for yaw, $I_{\mathrm{t}z}$ (t·m^2)	3.43
Mass of wheelset, M_{w} (t)	1.78
Mass moment of inertia of wheelset for roll, $I_{\mathrm{w}x}$ (t·m^2)	0.92
Mass moment of inertia of wheelset for pitch, $I_{\mathrm{w}y}$ (t·m^2)	0.30
Mass moment of inertia of wheelset for yaw, $I_{\mathrm{w}z}$ (t·m^2)	0.92
Longitudinal stiffness of primary suspension system dashpot, $K_{\mathrm{p}x}$ (kN/m)	332
Lateral stiffness of primary suspension system dashpot, $K_{\mathrm{p}y}$ (kN/m)	332
Vertical stiffness of primary suspension system dashpot, $K_{\mathrm{p}z}$ (kN/m)	900
Longitudinal damping of primary suspension system dashpot, $C_{\mathrm{p}x}$ (kN·s/m)	2
Lateral damping of primary suspension system dashpot, $C_{\mathrm{p}y}$ (kN·s/m)	2
Vertical damping of primary suspension system dashpot, $C_{\mathrm{p}z}$ (kN·s/m)	5
Longitudinal stiffness of secondary suspension system dashpot, $K_{\mathrm{s}x}$ (kN/m)	194
Lateral stiffness of secondary suspension system dashpot, $K_{\mathrm{s}y}$ (kN/m)	194
Vertical stiffness of secondary suspension system dashpot, $K_{\mathrm{s}z}$ (kN/m)	200
Longitudinal damping of secondary suspension system dashpot, $C_{\mathrm{s}x}$ (kN·s/m)	50
Lateral damping of secondary suspension system dashpot, $C_{\mathrm{s}x}$ (kN·s/m)	50
Vertical damping of secondary suspension system dashpot, $C_{\mathrm{s}z}$ (kN·s/m)	80

Table 2 Track parameters

Component	Item	Value
Rail	Elastic modulus (GPa)	210.0
	Density (kg/m^3)	60.64
	Poisson's ratio	0.33
Fastener	Vertical stiffness (N/m)	4.0×10^7
	Vertical damping (N·s/m)	4.9×10^5
	Bending stiffness (N·m^2)	2.95×10^4
	Bending damping (N·s·m^2)	1×10^5
Floating slab	Size (m)	3.40×2.60×0.34
	Elastic modulus (GPa)	34.5
	Density (kg/m^3)	2500.00
	Poisson's ratio	0.20
Shear hinge	Shear stiffness (N/m)	5×10^9
Steel spring	Vertical stiffness (N/m)	7.8×10^6
	Vertical damping (N·s/m)	6.0×10^4
Substrate	Size (m)	3.40×2.60×0.40
	Elastic modulus (GPa)	34.5
	Density (kg/m^3)	2500.00
	Poisson's ratio	0.20
Soil	Radial stiffness (N/m)	1.4×10^8
	Radial damping (N·s/m)	1.4×10^6
	Shear stiffness (N/m)	1×10^8
	Shear damping (N·s/m)	1×10^6

$$\tilde{\boldsymbol{M}}_{\mathrm{s}}\ddot{\boldsymbol{q}}_{\mathrm{s}i}(t)+\tilde{\boldsymbol{C}}_{\mathrm{s}}\dot{\boldsymbol{q}}_{\mathrm{s}i}(t)+\tilde{\boldsymbol{K}}_{\mathrm{s}}\boldsymbol{q}_{\mathrm{s}i}(t)=\tilde{\boldsymbol{F}}_{\mathrm{s}}(t), \tag{1}$$

where $\tilde{\boldsymbol{M}}_{\mathrm{s}}=\tilde{\boldsymbol{\Phi}}_{\mathrm{s}}^{\mathrm{T}}\boldsymbol{M}_{\mathrm{s}}\tilde{\boldsymbol{\Phi}}_{\mathrm{s}}$, $\tilde{\boldsymbol{C}}_{\mathrm{s}}=\tilde{\boldsymbol{\Phi}}_{\mathrm{s}}^{\mathrm{T}}\boldsymbol{C}_{\mathrm{s}}\tilde{\boldsymbol{\Phi}}_{\mathrm{s}}$, $\tilde{\boldsymbol{K}}_{\mathrm{s}}=\tilde{\boldsymbol{\Phi}}_{\mathrm{s}}^{\mathrm{T}}\boldsymbol{K}_{\mathrm{s}}\tilde{\boldsymbol{\Phi}}_{\mathrm{s}}$, and $\tilde{\boldsymbol{F}}_{\mathrm{s}}=\tilde{\boldsymbol{\Phi}}_{\mathrm{s}}^{\mathrm{T}}\boldsymbol{F}_{\mathrm{s}}$.

All frequencies of interest in this study were below 1000 Hz, and the frequency of the highest mode was much higher than 1000 Hz, which met the calculation accuracy requirements. The equations of motion were established and solved by the Zhai method, which is an explicit two-step numerical integration (Rio et al., 2005). Its basic form is shown in Eq. (2). The time step Δt was 0.0005 s, and the solution time length was 30 s. n refers to the nth time step. The integral constant φ was 0.5. $\boldsymbol{A}$, $\boldsymbol{X}$, and $\boldsymbol{V}$ refer to the acceleration, displacement, and velocity matrices, respectively. The initial position of the train was 253 m from the first slab, and the train speed was 65 km/h. Gravity pre-balance was carried out before the train's running. The forward direction of the train was defined as positive X-direction, the horizontal direction to the left-hand side of the forward train direction as positive Y-direction, and upward as the positive Z-direction.

$$\begin{cases} \boldsymbol{X}_{n+1} = \boldsymbol{X}_n + \boldsymbol{V}_n \Delta t + \left(\dfrac{1}{2} + \varphi \right) \boldsymbol{A}_n \Delta t^2 - \\ \qquad \varphi \boldsymbol{A}_{n-1} \Delta t^2, \\ \boldsymbol{V}_{n+1} = \boldsymbol{V}_n + (1+\varphi) \boldsymbol{A}_n \Delta t - \varphi \boldsymbol{A}_{n-1} \Delta t. \end{cases} \tag{2}$$

3 Dynamic response sensitivity to damage

Numerous physical quantities can describe the vertical motions of the floating slab, such as linear acceleration, velocity, displacement, angular displacement, angular velocity, and angular acceleration. Selecting physical quantities sensitive to steel spring failure can improve the damage identification accuracy. A failed spring was considered to have two states: complete failure, i.e., the steel spring is fully fractured, and partial failure, i.e., the steel spring is suspended. A partially failed, or suspended, steel spring may still provide some support to the floating slab. Both damage states are collectively referred to as failure in the following text. Slab No. 17 was the central one of all the floating slabs in the model and was the focus of analyses. Different slab No. 17 spring failure cases were considered and compared. All failures in this section are fracture for obvious comparison. The steel springs were numbered as shown in Fig. 4.

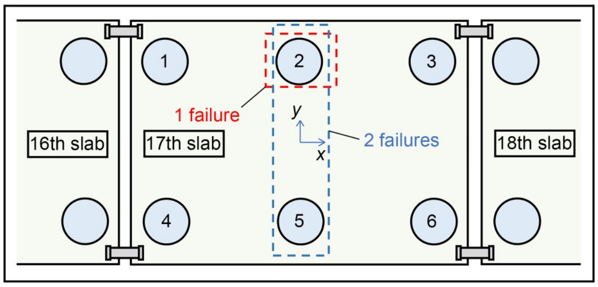

Fig. 4 Steel spring failure cases

The dynamic response results are shown in Fig. 5. In Figs. 5a and 5b, numerous signal bursts in acceleration and velocity can be seen, caused mainly by local impact, resulting in significant fluctuations in peak values. However, the RMS values are more stable. It can be seen that the fracture of a spring causes an increase in the RMS value, and the sensitivity of velocity to fracture is higher than that of acceleration. The displacement in Fig. 5c is smoother relative to acceleration and velocity, and the changes in peak and RMS values are more sensitive, evident, and stable. Figs. 5d and 5e show angular displacements with respect to the X- and Y-axes, respectively. Positive angular displacement satisfies the right-hand screw rule and is not sensitive to the fracture of the steel springs. However, in Fig. 5d, the angular displacement corresponding to one spring failure is the largest, and the fracture position is located in the positive Y-direction, which may suggest a technique for spring fracture location identification. As in translational motion, the angular displacement stability and sensitivity were higher than those of the angular velocity and acceleration, which are not shown here.

Fig. 5f shows the 1st-order vertical mode natural frequency of the floating slab. This vibration mode is the overall vertical resonance of the floating slab–steel spring system. The theoretical natural frequency was obtained by finite element modal analysis. The experimental frequency identified in the figure was obtained through operational modal analysis (OMA) and the data source came from Fig. 5a. This method can obtain the natural frequency from the dynamic response of the slab under external load excitation, avoiding separate modal tests such as hammer tests (Rajaram and Nelson, 2019). The modal identification was divided into two steps. Firstly, the free attenuation signal was extracted from the vertical acceleration time-domain signal, and then the modal parameters were calculated using a time-domain modal parameter identification method. Fig. 6 shows the main steps of modal parameter identification and the identified 1st-order natural frequency without failure. The random decrement technique (RDT) (Vandiver et al., 1982) only uses the center point data, while the natural excitation technique (NExT) (James III et al., 1995) uses the center point and corner point data. It can be seen that the differences in data handling by the different methods are the main cause of the difference in frequency identification. RDT is not suitable because the signal has no apparent attenuation, which is mainly caused by poor stability of train excitation. However, NExT uses more data and the identification results are very good. Autoregressive moving average model (ARMA) (Bertha and Golinval, 2017) and stochastic subspace identification (SSI) are more accurate for the preprocessed data. However, ARMA has fewer calculation steps and higher efficiency and is more suitable for processing data from many train runs. As shown in Fig. 5f, the difference between the calculation results using NExT/ARMA and the theoretical results is within 0.3 Hz. The theoretical and experimental identification

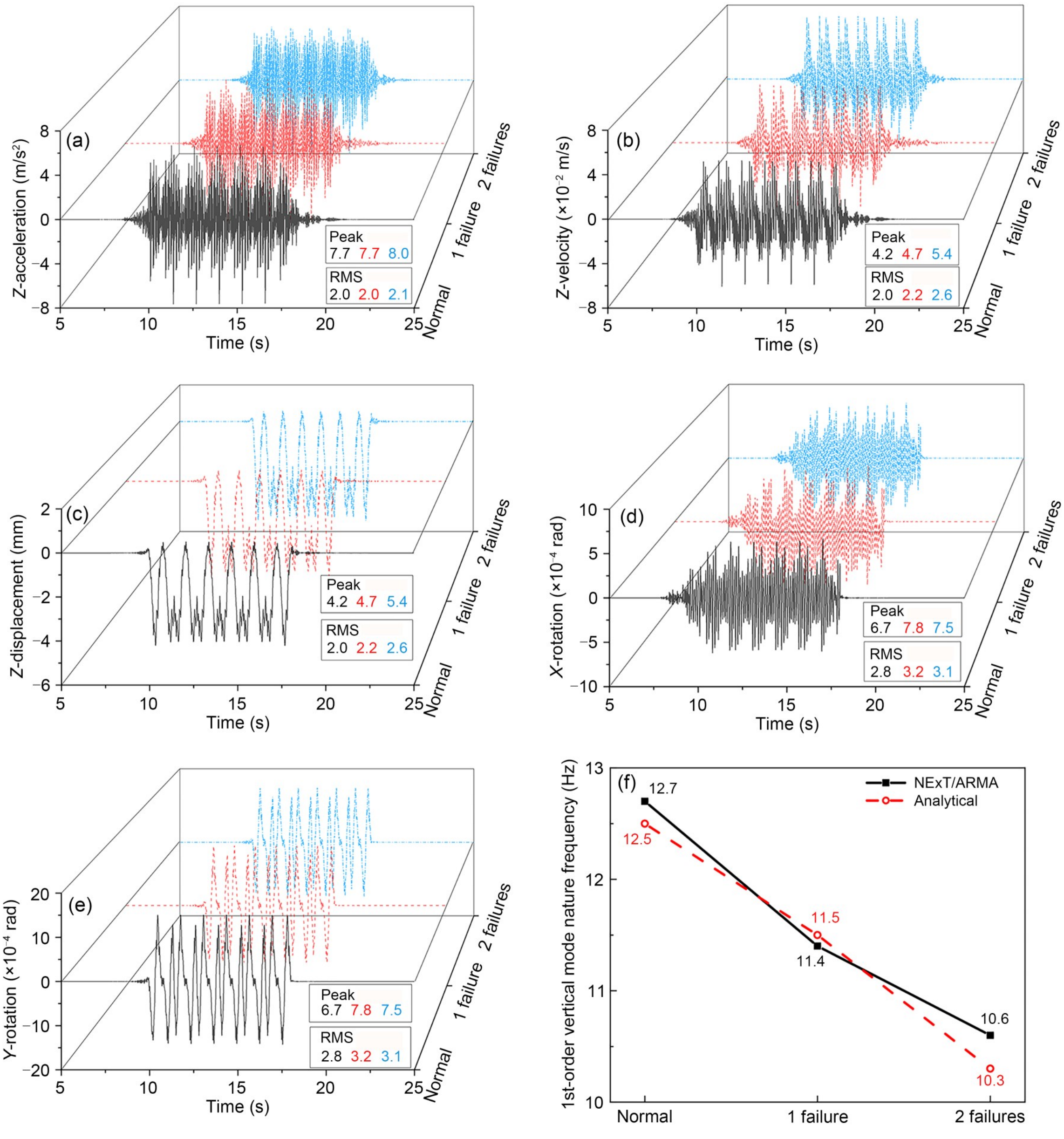

Fig. 5 Sensitivity analysis of dynamic response indices of slab No. 17: (a) vertical acceleration; (b) vertical velocity; (c) vertical displacement; (d) *X*-rotation; (e) *Y*-rotation; (f) 1st-order vertical mode natural frequency. References to color refer to the online version of this figure

results show that the 1st-order vertical mode natural frequency of the floating slab is sensitive to spring fracture.

4 Steel spring failure identification

4.1 Failure number identification

The 1st-order vertical mode natural frequency at different failure numbers, gaps, and positions is investigated in this section. The failure gap here refers to the vertical distance between the spring contact point and the floating slab after the system reaches static equilibrium under gravity. Different spring failure gaps for slab No. 17 were simulated by a nonlinear spring. Four failure gaps of 0, 2, 4, and 6 mm were considered, where 0 mm indicated that the failed spring was just in contact with the floating slab, and 6 mm meant the spring was broken because it could not contact the slab at all (Fig. 5c). The force–displacement relationships for steel springs with different failure gaps are

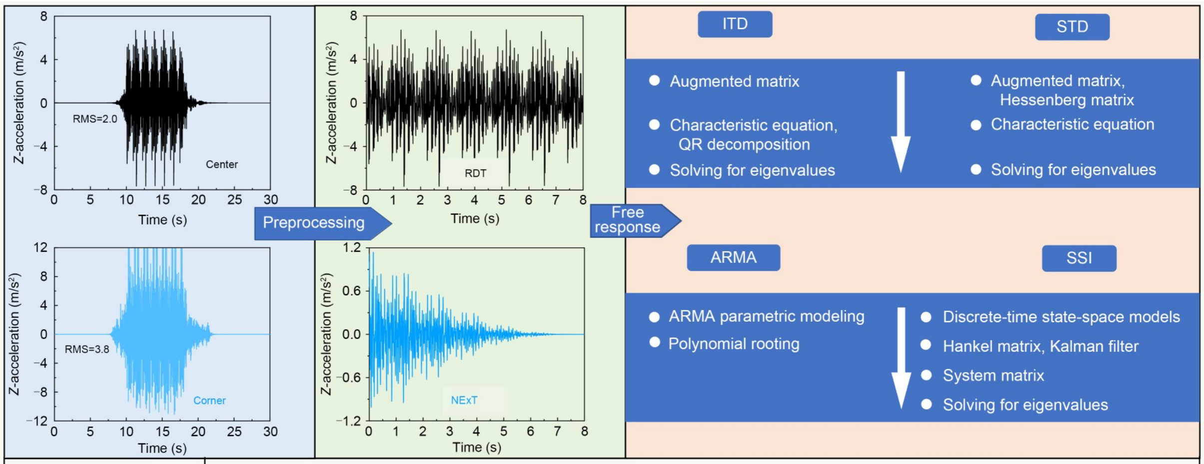

	Analytical	ITD	STD	ARMA	SSI
RDT	12.5	8.1	8.1	8.1	8.1
NExT	12.5	12.8	12.8	12.7	12.7

Fig. 6 Steps and results of natural frequency identification. ITD: Ibrahim time domain technique; STD: sparse time domain technique; QR: an orthonormal matrix *Q* and an upper triangular matrix *R*

illustrated in Fig. 7 and Table 3. The failure causes nonlinear behavior of the floating slab and it is challenging to solve the natural frequency by the finite element method. The modal identification method in the previous section can avoid this problem. This paper only studies the failure of one or two springs. Four failure cases are considered: spring No. 1 failed, spring No. 2 failed, springs Nos. 1 and 4 failed, and springs Nos. 2 and 4 failed. In the two-spring failure cases, e.g., springs Nos. 1 and 4 failed by 1 mm and 3 mm, respectively, the spring positions were noted as positions 14, and the gaps were abbreviated as 1+3.

The 1st-order slab vertical mode natural frequencies of different failure cases are shown in Table 3.

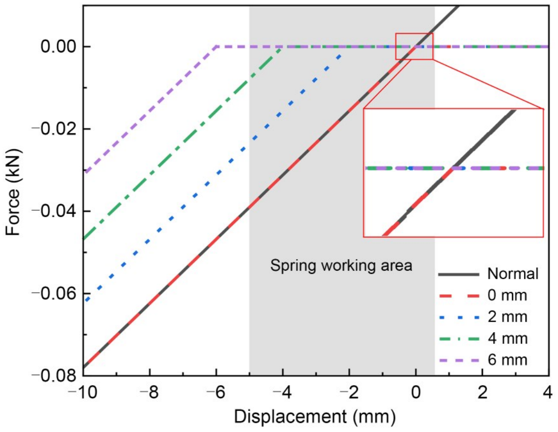

Fig. 7 Force–displacement relationships for steel springs with different failure gaps

Table 3 1st-order vertical mode natural frequencies of floating slab subjected to different combined failures

Gap (mm)	Frequency (Hz)			
	Position 1	Position 2	Positions 14	Positions 24
0	11.9	11.9		
2	11.4	11.5		
4	11.4	11.5		
6	11.4	11.4		
0+0			11.5	11.5
1+3			10.6	10.6
2+5			10.5	10.6
6+6			10.5	10.6
Normal	12.7	12.7	12.7	12.7

Each 1st-order frequency dropped significantly when the steel spring just failed (0 mm). After the failure gap exceeded 2 mm, the frequency gradually tended to the spring fracture frequency, which hardly changed with the failure gap. In addition, when the number of failed springs is the same, different failure gaps and positions had little effect on the frequency. This is because the failed spring can only be compressed and not stretched, equivalent to changing from a bidirectional spring to a unidirectional spring, which plays a significant role in the change of frequency. These characteristics show that the 1st-order vertical mode natural frequency can be used robustly to identify the number of failed springs.

4.2 Failure severity identification

The failure gap was used to quantify failure severity. Since the frequency was not sensitive to the failure gap, the maximum displacement was considered as an index to quantify the failure gap. Table 4 shows the peak displacements at various failure gaps. For one-spring failures, failure position No. 1 or No. 2 was selected. Before complete failure (gap<5 mm), there was a stable linear relationship between the displacement peak and the failure gap. For two-spring failure cases, the symmetrical case of positions 16 and asymmetrical case of positions 15 were selected. It can be seen that the different positions did not affect the maximum displacement in the case of two-spring failures. In addition, except for the case of 2+4, when the total failure gap of two springs was equal to the total failure gap of one spring, the maximum displacement of both springs was the same. This was because, in the case of 2+4, the two springs failed only partially, but in the case of one spring, 6 mm signified a complete failure. This indicates that the maximum dynamic displacement of the floating slab was only related to the total failure gap. However, when the failure gap changed, the displacement change rate was low. The on-site results will be further complicated because there are inevitable fluctuations in the actual track structure parameters. It was difficult to identify the failure gap accurately from displacements except when the failure gap was large.

Table 4 Maximum vertical dynamic displacements of floating slab subjected to different failures

Gap (mm)		Displacement (mm)			
		Position 2	Position 1	Positions 16	Positions 15
One spring damaged	0	4.2	4.2		
	2	4.4	4.4		
	4	4.7	4.6		
	6	4.7	4.6		
Two springs damaged	0+0			4.2	4.2
	1+1			4.4	4.4
	2+4			4.9	4.9
	6+6			5.2	5.2
Normal		4.2	4.2	4.2	4.2

4.3 Failure location identification

Based on the results shown in Fig. 5d, failure position identification from the rotation angle was attempted. Since the fluctuation of peak values was too large, the RMS of rotation angle was used. Two cases of one-spring failure, Nos. 1 and 2, were considered. Fig. 8 shows the RMS of each rotation direction in these two cases, where the purple solid line is the RMS of the rotation angle when there is no defect. Note that there are two types of RMS in Fig. 8. One is the RMS of the positive rotation part, and the other is the RMS of the negative rotation part. For example, 1: RMS+Y in Fig. 8a indicates the RMS of positive rotation angle around the Y-direction when spring No. 1 failed, while 2: RMS−X represents the RMS of the negative rotation angle around the X-direction when spring No. 2 failed. It can be seen from Figs. 8a and 8b that 1: RMS−Y>1: RMS+Y and 1: RMS−X>1: RMS+X in the case of spring No. 1 failure. This difference increased with the increase in the failure gap. In the case of spring No. 2 failure, 2: RMS−Y≈2: RMS+Y and 2: RMS−X>2: RMS+X. The above observations can be summarized as follows: if a spring in a specific direction fails, the rotation in this direction will increase. For other failure cases, such as spring No. 6 failure, a similar analysis can be conducted, which showed that 6: RMS−Y<6: RMS+Y and 6: RMS−X<6: RMS+X. The equivalence here assumes that the rotation angle is symmetric when there is no failure, which is confirmed by the purple line in Fig. 8a.

Failure of two springs can be analyzed in a similar way by division into six independent cases, as shown in Fig. 8c. Damage positions 1 and 2, 1 and 3, and 2 and 5 can be identified from the X- and Y-rotations. The remaining positions require special consideration. For positions 1 and 6, since the failure positions are centrosymmetric, the rotation should be considered as diagonal. Diagonal rotation can be calculated from the X- and Y-rotations. Note that the directions of diagonal lines for damage cases 16 and 43 are denoted as K and L, respectively (Fig. 8c). Considering the complete spring fracture at positions 16, the calculated RMS±K is 5.3×10^{-5} rad, and RMS±L is 4.4×10^{-5} rad, indicating that failure occurred at positions 1 and 6 instead of 3 and 4. For damage positions 1 and 4 and 1 and 5, their rotations in the X- and Y-directions are similar and should be judged in combination with the diagonal rotation. In case of complete failure, the RMS−K and RMS−L of positions 14 are both 6.6×10^{-4} rad, and the RMS−K and RMS−L of positions 15 are 5.4×10^{-4} and 4.8×10^{-4} rad. Therefore, it can be discerned whether the failure is in positions 14 or positions 15. Fig. 8d shows the rotations of the three exceptional cases.

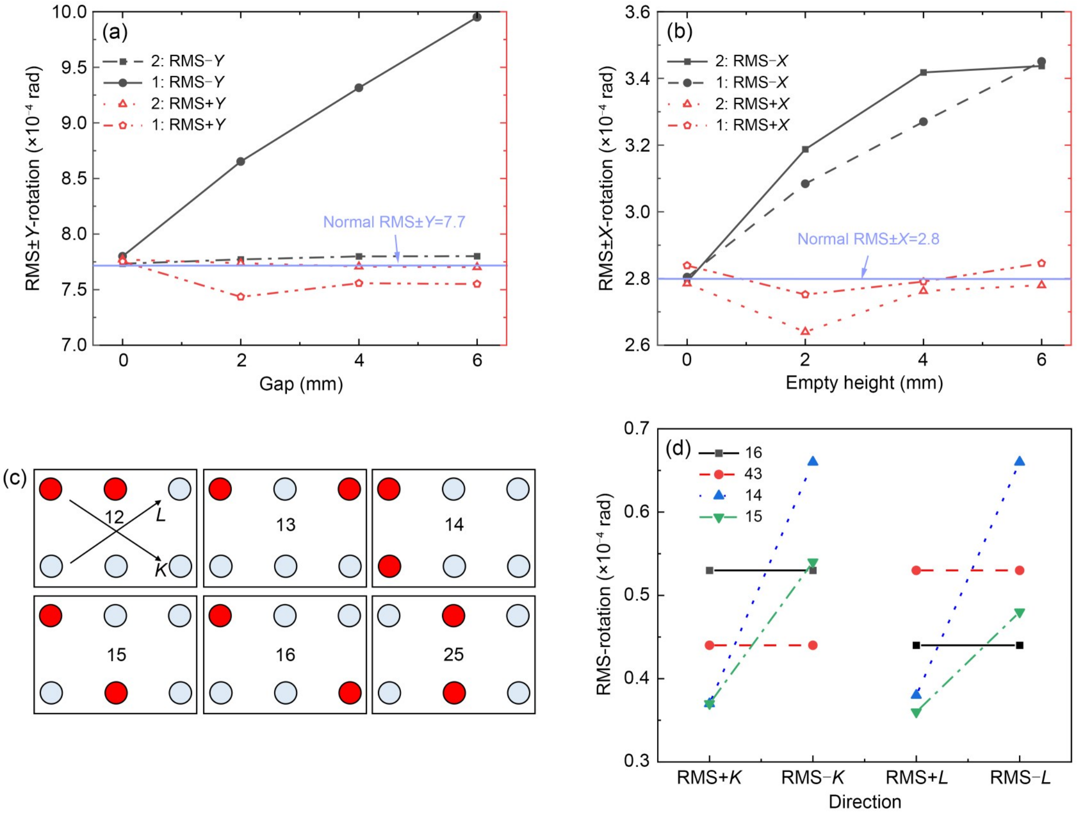

Fig. 8 Effective value of rotation angle for different failure positions: (a) RMS of *Y*-rotation; (b) RMS of *X*-rotation; (c) six cases for two-spring failures; (d) effective values of diagonal corner rotations in special cases. References to color refer to the online version of this figure

In summary, the failure positions can be identified as follows:

(1) For one-spring failure,

1: RMS−*X*>RMS+*X*, RMS−*Y*>RMS+*Y*;

2: RMS−*X*>RMS+*X*, RMS−*Y*≈RMS+*Y*.

(2) For two-spring failure,

12: RMS−*X*>RMS+*X*, RMS−*Y*>RMS+*Y*;

13: RMS−*X*>RMS+*X*, RMS−*Y*≈RMS+*Y*;

14: RMS−*X*≈RMS+*X*, RMS−*Y*>RMS+*Y*, RMS−*K*≈RMS−*L*;

15: RMS−*X*≈RMS+*X*, RMS−*Y*>RMS+*Y*, RMS−*K*>RMS−*L*;

25: RMS−*X*≈RMS+*X*, RMS−*Y*≈RMS+*Y*;

16: RMS−*K*>RMS−*L*.

5 Floating slab monitoring system

Based on the above analysis, the ISFST was proposed. The system has five parts: monitoring module, monitoring terminal, cloud server, data analysis system, and user terminal, as shown in Figs. 9 and 10. The monitoring module comprises sensors and communication units. The sensors are three-axial acceleration and three-axial angular velocity sensors. The communication unit includes a converter and a transmission cable. The converter changes analog electrical signals into digital ones. The transmission cable connects the monitoring module and the monitoring terminal. The monitoring terminal receives the digital signal from the monitoring module and transmits the data to the cloud server through a wireless network. The data analysis system processes the vibration data on the cloud server and then sends the data processing results to the user terminal. If the data is abnormal, the system automatically sends an alarm message to the user.

The system was successfully implemented on a section of a metro line in southern China. The radius of this rail line section is 390 m, the dimensions of the floating slab are 3.576 m×2.600 m×0.340 m, the gap between slabs is 12 mm, and the natural design frequency is 12.5 Hz. A monitoring module was arranged at the center of each slab. The monitoring area contains 16 boards, with a total length of about 60 m. The

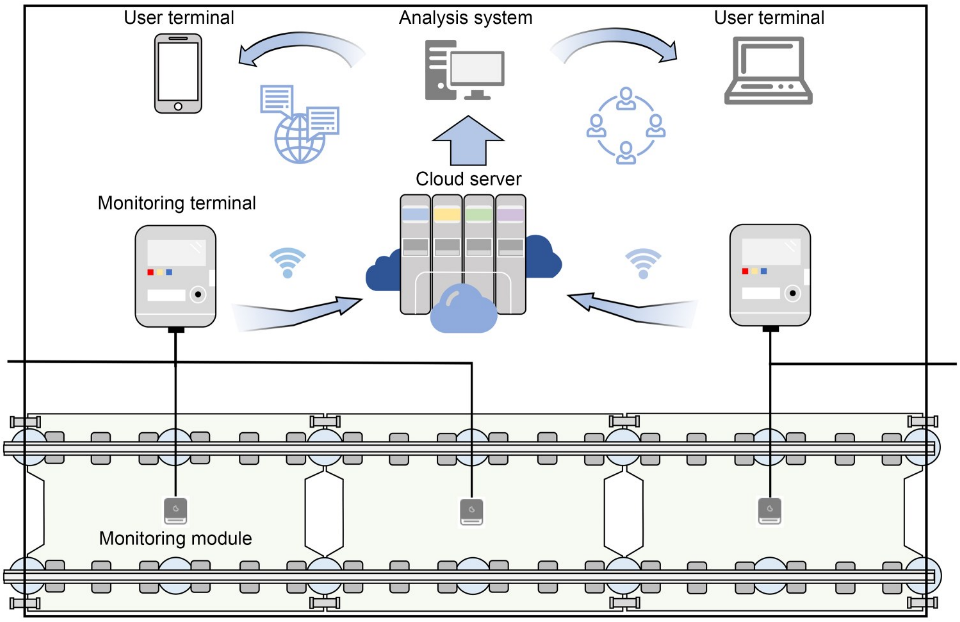

Fig. 9 Architecture of ISFST

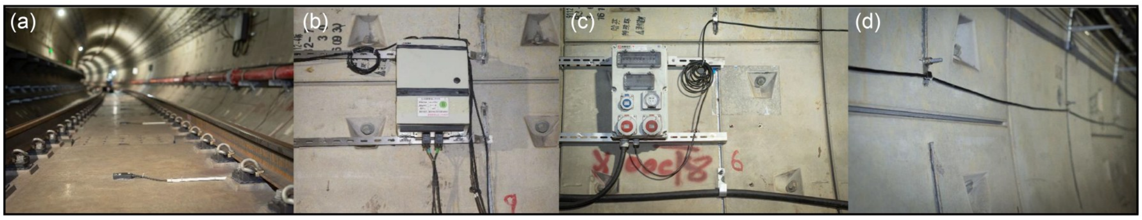

Fig. 10 On-site monitoring system: (a) monitoring module; (b) monitoring terminal; (c) power supply; (d) signal line

tunnel power supply was used to operate the entire monitoring system. Slightly different from the above theoretical analysis, the vibration isolators at the adjacent slab ends support the two adjacent floating slabs simultaneously and their stiffness is about twice that of the steel springs in the middle of the slab. Although this section is located on a curve, this does not affect the above identification rules. The functions of the monitoring system include more than steel spring condition monitoring. The training data can be obtained by analyzing the responses of the floating slabs caused by different train runs. The rail status can be monitored by comparing the responses of floating slabs at different times caused by the same train type. However, this study only focuses on the steel spring support stiffness monitoring.

In view of many interference factors existing during the actual on-site operation, the damage identification method proposed above may yield erroneous results. Compared to identifying the number, severity, and location of failures, the most critical task is detecting failure presence. On the other hand, we hope that the identification efficiency is high and failure can be found using a small amount of data. Therefore, it is necessary to strengthen the system's ability to identify abnormal data. Abnormal data identification usually adopts cluster analysis or statistical methods. The proposed system combines cluster analysis and statistical methods, using the density-based spatial clustering of applications with noise (DBSCAN) algorithm to judge failure (whether there is a failure) and statistical analysis to identify failure (detailed information on the failure). DBSCAN is a density-based clustering algorithm that can identify noise and outliers and is suitable for the classification of various patterns present in the database (Li, 2020). The 1st-order vertical mode natural frequency of the floating slab (f), the maximum vertical dynamic displacement (Z), and the difference in the RMS values (R) are extracted from the original data. The difference between the effective values of rotations includes three categories: (RMS−X)−(RMS+X), (RMS−Y)−(RMS+Y), and (RMS+K)−(RMS+L). They are abbreviated as R_X, R_Y, and R_{KL}, respectively. To reduce the data dimension, an equivalent rotation was introduced, which was defined as $R_{\mathrm{E}}=\sqrt{\overline{R_X}^2+\overline{R_Y}^2+\overline{R_{KL}}^2}$. The minimum-maximum normalized values were denoted as $\bar{f}$, $\overline{Z}$, and $\overline{R_{\mathrm{E}}}$. The DBSCAN algorithm was used to cluster the 3D data. The domain radius, E_{ps}, was then selected as follows (Collier, 2003):

$$E_{\mathrm{ps}}=\left(\frac{\lambda N_{\min}\Gamma\left(\frac{n}{2}+1\right)}{m\sqrt{\pi^n}}\right)^{\frac{1}{n}}, \tag{3}$$

where m represents the total number of samples, Γ is the Gamma function, $n=3$ represents the data dimension, $N_{\min}=5$ represents the minimum number of cluster points, and $\lambda=(\max(\bar{f})-\min(\bar{f}))\cdot(\max(\overline{Z})-\min(\overline{Z}))\cdot(\max(\overline{R_{\mathrm{E}}})-\min(\overline{R_{\mathrm{E}}}))$.

Fig. 11 shows the clustering results of the data from 20 train runs at the beginning of the system operation. There were two types of data. Type I is all the data of slab No. 4, but a few data of slab No. 4 are classified as type II (outliers), indicating that a steel spring in slab No. 4 was damaged. As shown in Fig. 11b, although the planar projections of two types of data overlapped, the method achieved satisfactory results using three types of data (Fig. 11a), which shows that the method can reduce the impact of single-type data fluctuations on failure identification. This method was still very effective for data clustering from one train run, which shows that this method can effectively find failures.

The failure characteristics were identified by statistical analysis. Fig. 12 shows the average value of all data on a particular day at the beginning of system operation, and the shaded area represents the standard deviation. It can be seen from Fig. 12a that the frequency of slab No. 4 was much lower than that of other slabs, indicating that the support stiffness was insufficient, which may be due to the suspension of the support or the fracture of the steel spring. Compared to the design frequency, the frequency of slab No. 4 has decreased by 1.4 Hz. According to Fig. 5f, there is a high probability of one failure. The dynamic displacement of slab No. 4 shown in Fig. 12b was high, and the difference from other slabs was almost 0.5 mm. Based on these observations, it was speculated that lifting might have occurred. Figs. 12c and 12d show the difference between each slab RMSs of positive and negative rotations. It is evident that for slab No. 4, RMS+X>RMS−X and RMS+Y<RMS−Y. Therefore, the failure position identified by the monitoring system was the shared isolator of slabs Nos. 3 and 4, located to the right-hand side of the forward direction, and the suspension gap was 2–4 mm. In addition, the natural frequency of slab No. 3 was high, while its displacement was low, which was consistent with this conclusion. The system sent an alert message to the users.

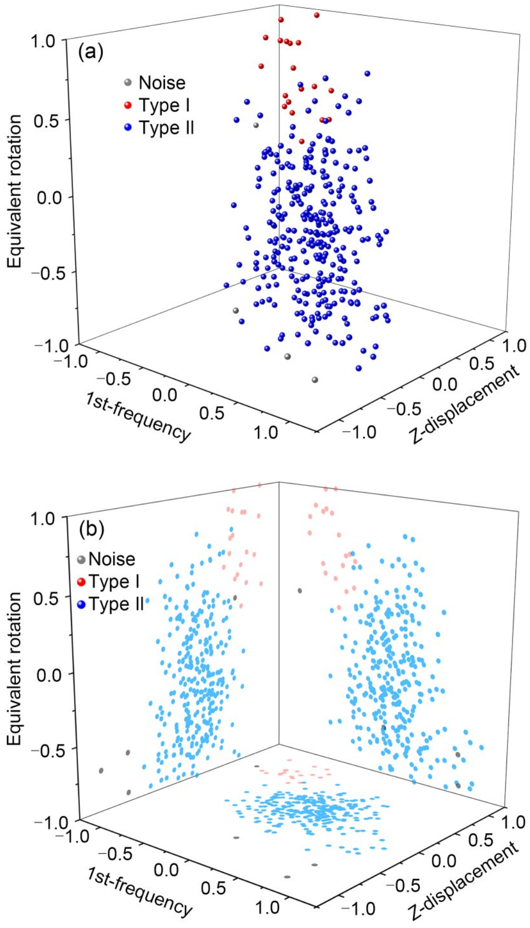

Fig. 11 Cluster analysis based on sensitive response indices: (a) space distribution; (b) projection in *XYZ*. References to color refer to the online version of this figure

After a field inspection performed by maintenance personnel, it was found that the shared isolator of slabs Nos. 3 and 4 had failed. The failure gap was about 2–3 mm, and a steel ruler with a thickness of 1.5 mm could be inserted. The isolator was repaired by adding vibration isolation gaskets, and the natural frequency of slab No. 4 was monitored the next day. It was found that the frequency had returned to the normal value, as shown in Fig. 13.

In the following three years of long-term monitoring, the system also identified a steel spring fracture damage and cluster analysis quickly found that the abnormality was located in slab No. 7. Statistical analysis showed that steel spring No. 2 in slab No. 7 was broken. Since the process was similar to the above suspension failure identification, only the 1st-order vertical mode natural vibration frequency and vertical dynamic displacement are shown here. Based on the frequency

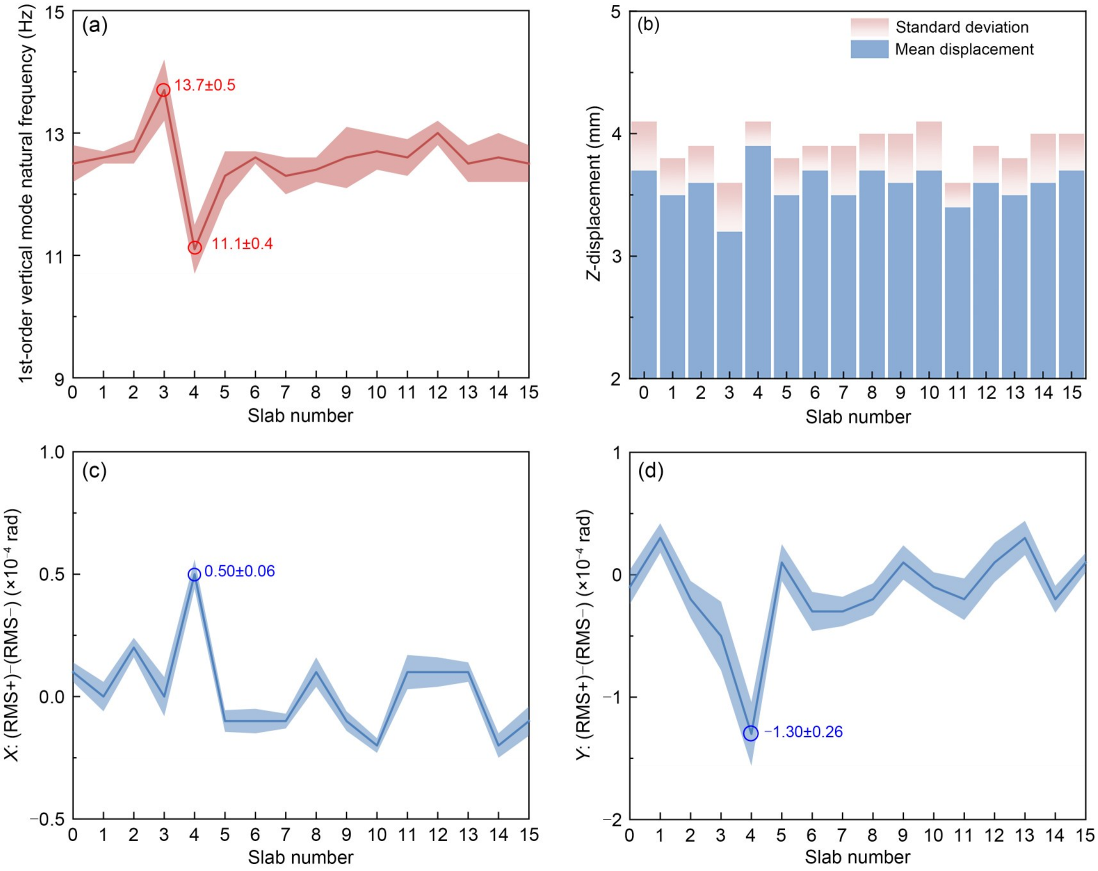

Fig. 12 Damage indices of floating slab: (a) 1st-order vertical mode natural frequency; (b) vertical dynamic displacement; (c) difference in effective values of rotation angles in *X*-direction; (d) difference in effective values of rotation angles in *Y*-direction

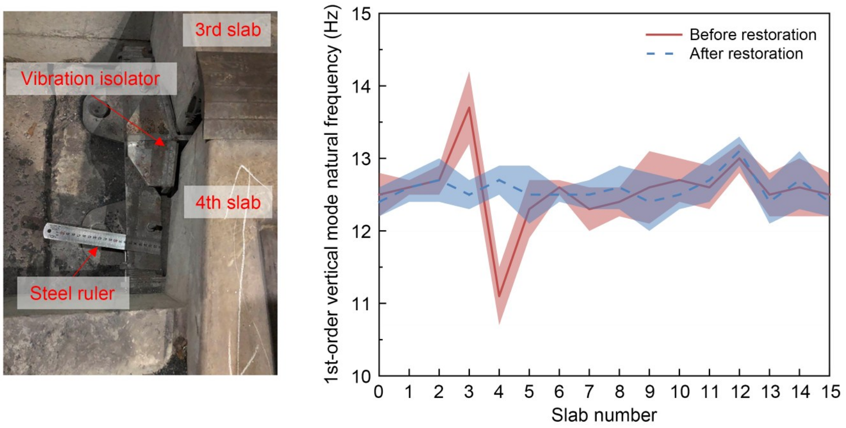

Fig. 13 On-site confirmation of steel spring hoisting

difference, it could be determined that the number of failures was 1. Sensitivity analysis showed that the maximum dynamic displacement was the main difference between steel spring fracture and suspension data. The dynamic displacement of slab No. 7 in Fig. 14b was almost 0.5 mm higher than that of other slabs, so the possibility of fracture was high. The identification results were confirmed on-site, as shown in Fig. 15. After the damaged steel spring was removed and replaced with a new one, the natural frequency returned to the pre-damage value.

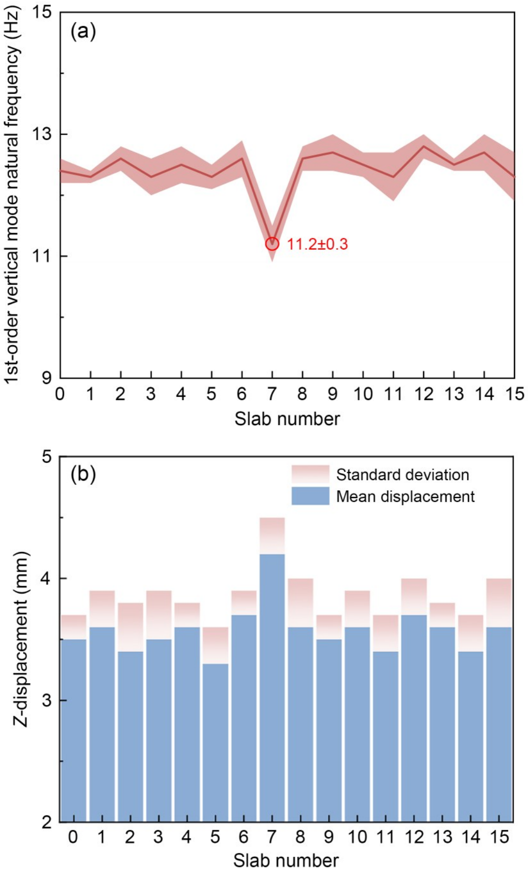

Fig. 14 Damage indices of floating slab: (a) 1st-order vertical mode natural frequency of floating slab; (b) vertical dynamic displacement

6 Conclusions

This study was concerned with the problem of steel spring failures in steel spring floating slab tracks. It established a refined coupled train-floating slab track-foundation analytical model and analyzed the sensitivity of several dynamic response indices of a floating slab to failure. Adopting the damage-sensitive physical quantities, a method for identifying the number, severity, and location of steel spring failures was proposed. Based on this method, the ISFST was established and installed on a rail line in southern China. Cases of steel spring suspension and fracture were successfully identified and detailed failure information was obtained.

The sensitivity analysis of the dynamic model responses showed that the 1st-order vertical mode natural frequency, the maximum vertical dynamic displacement, and the RMS of the rotation of the floating slab under the train loads are easily affected by steel spring failures. The specific features are as follows:

1. The experimental 1st-order vertical mode natural frequency of the floating slab under train load was obtained using the NExT/ARMA algorithms. This index is most sensitive to the number of failed springs but is insensitive to the spring failure gap or failure

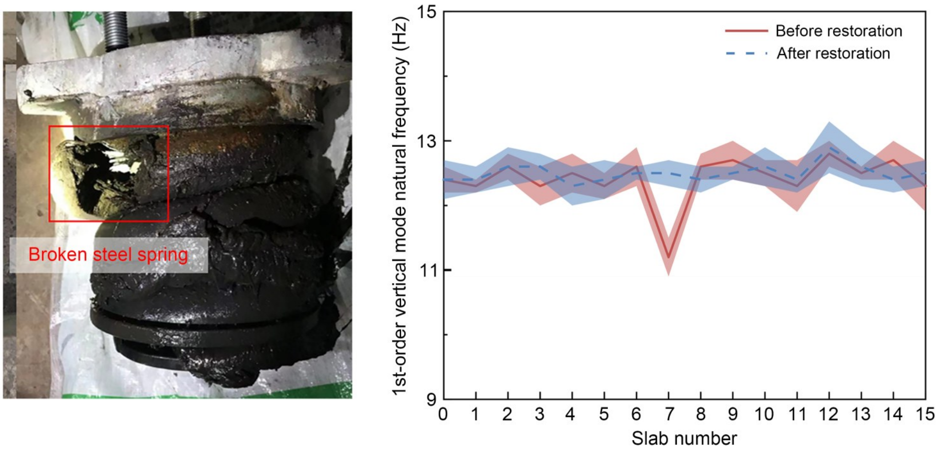

Fig. 15 On-site confirmation of steel spring fracture

location. Thus, it can be used to determine the number of failed steel springs.

2. The maximum vertical dynamic displacement has an excellent linear relationship with the total failure gap, but is relatively unaffected by the specific distribution of the locations of failed springs. Due to the complexity of track parameters, it is difficult to identify the failure gap accurately but it can nevertheless be roughly estimated.

3. The RMS of the response angles is susceptible to the number, severity, and location of failures. However, the magnitudes of the practical values of the rotation angles are very stable for the specific distribution of failure positions, enabling the failure position to be determined.

According to the above observations, a set of identification methods for steel spring failure was established. Firstly, the number of failures was determined using the identified 1st-order vertical mode natural frequency and then the failure severity was determined from the maximum vertical dynamic displacement. The failure position was obtained from the RMS of the rotations in each direction. This study considered only the damage location identification of one or two springs.

Using the above methods, the ISFST was established utilizing the DBSCAN algorithm and statistical analysis and used successfully to detect the failures of steel springs on-site, which were consistent with the field investigation results. After repair, the 1st-order vertical mode natural frequency returned to its pre-damage average level.

In addition to the steel spring failure mentioned in this study, there are also shear hinge fractures and fastener failures in floating slab track. The identification of these defects is worth further research.

Acknowledgments

This work is supported by the National Natural Science Foundation of China (Nos. 51978585 and 52008264), the Applied Basic Research Programs of Science and Technology Commission Foundation of Sichuan Province (No. 2020YJ0214), the Foundation of High-speed Rail Joint Fund Key Projects of Basic Research (No. U1734207), and the Foundation of National Engineering Laboratory for Digital Construction Evaluation Technology of Urban Rail Transit, China (No. 2023JZ01).

Author contributions

Junyuan ZHENG designed the research. Caiyou ZHAO, Jian WANG, and Bolong JIANG processed the corresponding data. Junyuan ZHENG wrote the first draft of the manuscript. Duojia SHI, Ping WANG, and Xi SHENG helped to organize the manuscript. Junyuan ZHENG revised and edited the final version.

Conflict of interest

Junyuan ZHENG, Caiyou ZHAO, Duojia SHI, Ping WANG, Jian WANG, Bolong JIANG, and Xi SHENG declare that they have no conflict of interest.

References

Ankrah AA, Kimotho JK, Muvengei OM, 2020. Fusion of model-based and data driven based fault diagnostic methods for railway vehicle suspension. *Journal of Intelligent Learning Systems and Applications*, 12(3):51-81. https://doi.org/10.4236/jilsa.2020.123004

Auersch L, 2017. Static and dynamic behaviours of isolated or unisolated ballast tracks using a fast wavenumber domain method. *Archive of Applied Mechanics*, 87(3):555-574. https://doi.org/10.1007/s00419-016-1209-6

Bashir S, Akhtar N, 2022. Development of low-frequency mass spring system for underground high-speed railways. *Journal of Vibration Engineering & Technologies*, 10(2):559-579. https://doi.org/10.1007/S42417-021-00392-W

Bertha M, Golinval JC, 2017. Identification of non-stationary dynamical systems using multivariate ARMA models. *Mechanical Systems and Signal Processing*, 88:166-179. https://doi.org/10.1016/j.ymssp.2016.11.024

Chandran P, Thiery F, Odelius J, et al., 2022. Unsupervised machine learning for missing clamp detection from an in-service train using differential eddy current sensor. *Sustainability*, 14(2):1035. https://doi.org/10.3390/su14021035

Collier M, 2003. A micro-AGV for flexible manufacturing in small enterprises. *Integrated Manufacturing Systems*, 14(5):442-448. https://doi.org/10.1108/09576060310477843

Cong JL, Gao MY, Wang Y, et al., 2020. Subway rail transit monitoring by built-in sensor platform of smartphone. *Frontiers of Information Technology & Electronic Engineering*, 21(8):1226-1238. https://doi.org/10.1631/FITEE.1900242

Cui XL, Chen GX, Yang HG, et al., 2016. Study on rail corrugation of a metro tangential track with Cologne-egg type fasteners. *Vehicle System Dynamics*, 54(3):353-369. https://doi.org/10.1080/00423114.2015.1137955

Dersch MS, Khachaturian C, Edwards JR, 2021. Methods to mitigate railway premium fastening system spike fatigue failures using finite element analysis. *Engineering Failure Analysis*, 121:105160. https://doi.org/10.1016/j.engfailanal.2020.105160

Dilena M, Limongelli MP, Morassi A, 2015. Damage localization in bridges via the FRF interpolation method. *Mechanical Systems and Signal Processing*, 52-53:162-180. https://doi.org/10.1016/j.ymssp.2014.08.014

Gomes GF, Giovani RS, 2022. An efficient two-step damage

identification method using sunflower optimization algorithm and mode shape curvature (MSDBI–SFO). *Engineering with Computers*, 38(2):1711-1730.
https://doi.org/10.1007/s00366-020-01128-2

Hong N, Li LS, Yao WR, et al., 2020. High-speed rail suspension system health monitoring using multi-location vibration data. *IEEE Transactions on Intelligent Transportation Systems*, 21(7):2943-2955.
https://doi.org/10.1109/tits.2019.2921785

James III GH, Carne TG, Laufer JP, 1995. The natural excitation technique (NExT) for modal parameter extraction from operating structures. *Modal Analysis: The International Journal of Analytical and Experimental Modal Analysis*, 10(4):260-277.

Lam HF, Wong MT, Yang YB, 2012. A feasibility study on railway ballast damage detection utilizing measured vibration of in situ concrete sleeper. *Engineering Structures*, 45:284-298.
https://doi.org/10.1016/j.engstruct.2012.06.022

Li SS, 2020. An improved DBSCAN algorithm based on the neighbor similarity and fast nearest neighbor query. *IEEE Access*, 8:47468-47476.
https://doi.org/10.1109/ACCESS.2020.2972034

Li ZW, Liu XZ, Lu HY, et al., 2020. Surface crack detection in precasted slab track in high-speed rail via infrared thermography. *Materials*, 13(21):4837.
https://doi.org/10.3390/ma13214837

Loveday PW, Long CS, Ramatlo DA, 2020. Ultrasonic guided wave monitoring of an operational rail track. *Structural Health Monitoring*, 19(6):1666-1684.
https://doi.org/10.1177/1475921719893887

Nelson JT, Watry DL, Amato MA, et al., 2018. Sound transit prototype high performance low frequency floating slab testing and evaluation. *In*: Anderson D, Gautier PE, Iida M, et al. (Eds.), Noise and Vibration Mitigation for Rail Transportation Systems. Springer, Heidelberg, Germany, p.607-618.
https://doi.org/10.1007/978-3-319-73411-8_48

Rajaram S, Nelson JT, 2019. High-performance floating slab track: design and construction improvements based on lessons learned from prototype slabs. *Transportation Research Record: Journal of the Transportation Research Board*, 2673(1):300-309.
https://doi.org/10.1177/0361198118823004

Ramos A, Correia AG, Calçada R, et al., 2021. Influence of track foundation on the performance of ballast and concrete slab tracks under cyclic loading: physical modelling and numerical model calibration. *Construction and Building Materials*, 277:122245.
https://doi.org/10.1016/j.conbuildmat.2021.122245

Rio G, Soive A, Grolleau V, 2005. Comparative study of numerical explicit time integration algorithms. *Advances in Engineering Software*, 36(4):252-265.
https://doi.org/10.1016/j.advengsoft.2004.10.011

Shen ZY, Hedrick JK, Elkins JA, 1983. A comparison of alternative creep force models for rail vehicle dynamic analysis. *Vehicle System Dynamics*, 12(1-3):79-83.
https://doi.org/10.1080/00423118308968725

Sitharam TG, Sebastian R, Fazil F, 2018. Vibration isolation of buildings housed with sensitive equipment using open trenches–case study and numerical simulations. *Soil Dynamics and Earthquake Engineering*, 115:344-351.
https://doi.org/10.1016/j.soildyn.2018.08.033

Talbot JP, 2016. Base-isolated buildings: towards performance-based design. *Proceedings of the Institution of Civil Engineers-Structures and Buildings*, 169(8):574-582.
https://doi.org/10.1680/jstbu.15.00057

Tamagawa S, 2021. Determination of load test conditions for rail fastenings of a floating slab track. *International Journal of Computational Methods and Experimental Measurements*, 9(1):14-27.
https://doi.org/10.2495/CMEM-V9-N1-14-27

Vandiver JK, Dunwoody AB, Campbell RB, et al., 1982. A mathematical basis for the random decrement vibration signature analysis technique. *Journal of Mechanical Design*, 104(2):307-313.
https://doi.org/10.1115/1.3256341

Wang L, Zhao YN, Sang T, et al., 2022. Ultra-low frequency vibration control of urban rail transit: the general quasi-zero-stiffness vibration isolator. *Vehicle System Dynamics*, 60(5):1788-1805.
https://doi.org/10.1080/00423114.2021.1874428

Wickramasinghe WR, Thambiratnam DP, Chan THT, 2020. Damage detection in a suspension bridge using modal flexibility method. *Engineering Failure Analysis*, 107:104194.
https://doi.org/10.1016/j.engfailanal.2019.104194

Wilson GP, Saurenman HJ, Nelson JT, 1983. Control of groundborne noise and vibration. *Journal of Sound and Vibration*, 87(2):339-350.
https://doi.org/10.1016/0022-460X(83)90573-4

Xu FZ, Song XL, Yang JJ, 2020. Influence of steel spring failure of floating slab track on vibration characteristics of infrastructure. *In*: Tutumluer E, Chen XB, Xiao YJ (Eds.), Advances in Environmental Vibration and Transportation Geodynamics. Springer, Singapore, p.987-998.
https://doi.org/10.1007/978-981-15-2349-6_67

Yu P, Manalo A, Ferdous W, et al., 2021. Failure analysis and the effect of material properties on the screw pull-out behaviour of polymer composite sleeper materials. *Engineering Failure Analysis*, 128:105577.
https://doi.org/10.1016/j.engfailanal.2021.105577

Yuan XC, Zhu SY, Xu L, et al., 2020. Investigation of the vibration isolation performance of floating slab track with rubber bearings using a stochastic fractional derivative model. *Proceedings of the Institution of Mechanical Engineers, Part F: Journal of Rail and Rapid Transit*, 234(9):992-1004.
https://doi.org/10.1177/0954409719883552

Zhao CY, Liu DY, Zhang XM, et al., 2019. Influence of vibration isolator failure on vehicle operation performance and floating slab track structure vibration reduction effectiveness. *Shock and Vibration*, 2019:8385310.
https://doi.org/10.1155/2019/8385310

Zhao CY, Zheng JY, Sang T, et al., 2021. Computational analysis of phononic crystal vibration isolators via FEM coupled

with the acoustic black hole effect to attenuate railway-induced vibration. *Construction and Building Materials*, 283:122802.
https://doi.org/10.1016/j.conbuildmat.2021.122802

Zhu SY, Zhang QL, Zhai WM, et al., 2021. Sensor deploying for damage identification of vibration isolator in floating-slab track using deep residual network. *Measurement*, 183:109801.
https://doi.org/10.1016/j.measurement.2021.109801

Zou JH, Du TF, Chen W, et al., 2022. Experimental study of concrete floating slab municipal road with steel spring isolators under vehicle loads. *Construction and Building Materials*, 315:125686.
https://doi.org/10.1016/j.conbuildmat.2021.125686